Journal of Sound and Vibration 546 (2023) 117419

Contents lists available at ScienceDirect

Journal of Sound and Vibration

journal homepage: www.elsevier.com/locate/jsvi

Efficient shear layer corrections for acoustics in arbitrary jet flows

J. Biesheuvel [a,b,*], M. Tuinstra [a], L.D. de Santana [b], C.H. Venner [b]

[a] Royal Netherlands Aerospace Centre, Department of Vertical Flight and Aeroacoustic, the Netherlands
[b] University of Twente, Department of Thermal and Fluid Engineering, Engineering Fluid Dynamics research group, the Netherlands

ARTICLE INFO

Keywords:
Beamforming
Microphone array
Acoustic delay
Acoustic propagation time
Fermat's principle
Shear layer

ABSTRACT

Localization of aeroacoustic sound sources in open jet wind tunnel experiments requires an accurate prediction of the acoustic propagation time. Most conventional predictions use either a ray-tracer, coupled with a modelled continuous velocity field, or use ray diffraction and a discretization of the velocity field by means of vortex sheets. In this work a novel method is proposed in which the continuous velocity field is discretized into blocks of constant velocity separated by velocity discontinuities, thus removing the requirement for the velocity to be parallel to the surface that separates the blocks. The acoustic ray is solved by minimization of the acoustic propagation time. The computational effort is low compared to ray-tracing methods while maintaining an improvement in accuracy compared to methodologies using vortex sheets. A specific continuous velocity field is derived that models a self-similar shear layer expanding asymmetrically from a rectangular nozzle. Subsequently, this velocity field is discretized to compute the acoustic rays. Experimental results with a loudspeaker source placed in the open jet of a large industrial wind tunnel showed a decrease in source localization uncertainty compared to techniques based on vortex sheets. This is attributed to the inclusion of the shear layer slanting.

1. Introduction

Society requires more renewable energy production from wind turbines. In addition there is increased demand for transportation of goods and people by aircraft. Both wind turbines and aircraft should be as quiet as possible. To achieve this the design of wind turbines and aircraft is aided by experiments performed in aeroacoustic wind tunnels. The wind tunnel experiments entail the recording of the sound by arrays of microphones which allows to predict and study the noise emitted from the final product. Microphone signals may be processed further in order to localize the sound sources. The localization algorithms rely on accurate predictions of the acoustic propagation time from the sound source to the microphones. Computation of an accurate propagation time with minimal computational effort is therefore an important step towards reduced noise pollution.

Performing the experiment in aeroacoustic wind tunnels is important because these wind tunnels combine aerodynamic and acoustic characteristics essential to the development of silent technologies [1,2] and research concerning aerodynamic sound production phenomena and noise abatement techniques [3]. Aeroacoustic facilities support the development of aviation [4–6], wind energy [7–9] and the emerging industry of urban aerial mobility [10,11]. Aeroacoustic testing facilities feature different types of test sections, namely, open, closed and hybrid [12–14]. Each test section type has specific advantages and limitations [15,16], yielding different results [17,18]. In particular, aeroacoustic wind tunnels with an open test section are used to measure the far-field radiation of a sound source under free-field conditions. In the far-field the distance r to a compact source is much larger than the wavelength λ

* Corresponding author at: University of Twente, Department of Thermal and Fluid Engineering, Engineering Fluid Dynamics research group, the Netherlands.
E-mail address: j.biesheuvel@utwente.nl (J. Biesheuvel).

https://doi.org/10.1016/j.jsv.2022.117419
Received 17 March 2022; Received in revised form 10 August 2022; Accepted 1 November 2022
Available online 11 November 2022

Nomenclature

c_e	Effective speed of sound [–]
c_T	Thermodynamic speed of sound [ms^{-1}]
f	Frequency [s^{-1}]
H	Nozzle height [m]
$\boldsymbol{J}$	Action [–]
L	Wind tunnel reference length [m]
$\mathcal{L}$	Lagrangian [–]
$\boldsymbol{M}$	Mach vector [–]
$\boldsymbol{n}$	Vector normal to wave front [–]
p	Power function [–]
$\boldsymbol{r}$	Ray point location [–]
s	Arc length [–]
t	Time [s]
T	Total propagation time [s]
$\overline{U}$	Mean flow velocity [ms^{-1}]
W	Nozzle width [m]
$\boldsymbol{x}$	Spatial location [m]
γ	Prandtl–Glauert factor [–]
$\delta \ldots$	Functional variation of …
η	Self-similar parameter [–]
$\hat{\eta}$	Optimal flow division parameter [–]
λ	Wave length [m]
$\boldsymbol{\Phi}$	Phase function [–]
τ	Dimensionless time [–]

and the pressure decays as $1/r$. In general, aeroacoustic noise sources do not radiate sound equally in every direction. Therefore, an open test section is ideal for measuring the far-field radiation because the wall can be acoustically treated to avoid reflections. This simulates a free-field environment whereby only the noise characteristics of the subject are measured. Furthermore, the microphones can be located sufficiently far from the noise source at different observer angles, making the open jet flow configuration the most adequate for the quantification of the far-field radiation of the aeroacoustic sources.

Large-scale industrial wind tunnels are necessary for testing new products at a high Reynolds number, e.g., aeroacoustic tests on aircraft models [19]. The dependence of the acoustics on the Reynolds number is important both for Aeolian tones and broadband noise [20]. For a simple Helmholtz scaling the frequencies of interest can become so high that it becomes a challenge to accurately measure the acoustics of the source due to the presence of background noise and wave–turbulence interactions. Even for a moderate scaling of 1:10 the frequencies can already span a range up to 50 kHz while the model span is still in the order of meters. Large wind tunnels also allow for full scale tests on many transportation vehicles, e.g., trucks and trains [21], or wing sections from a wind turbine [22]. This eliminates any scaling uncertainties or geometry related fidelity uncertainties, e.g., missing bolts or slots.

Correcting the acoustic measurement for the presence of the wind tunnel shear layer is essential for an accurate prediction of the free-field radiation of the full-scale product. Fig. 1(a) shows a schematic of a typical test with an aircraft model placed in the wind tunnel jet and the microphone array standing in the quiescent air. The jet and quiescent air are separated by the shear layer. For large industrial wind tunnels the shear layer thickness can reach up to 1 m. To compare acoustic wind tunnel measurements to free-field radiation emission-angle corrections are applied. Furthermore, phased array techniques, in particular the beamforming method, use predictions of the acoustic propagation path to localize the sound sources and quantify the source power. Generally, more accurate predictions of the acoustic propagation time decrease the uncertainty of the sound source location.

The current state-of-the-art correction methodologies for acoustic propagation can be classified as purely analytical methods, computational aeroacoustics (CAA), and hybrid methods, sometimes coupled with computational fluid dynamics (CFD). Conventional methodologies assume the acoustic pressure to be small and therefore use the theory of linear acoustics. Additional simplifications can be made by assuming a high frequency sound source. Within this high frequency assumption the Eikonal equation [23] describes the propagation of the acoustic wavefront. The characteristics of the Eikonal equation equal the paths of the acoustic rays, hence the approach is also known as geometrical acoustics. The Eikonal equation's characteristics can be solved as an initial value problem in which a numerical solver iteratively searches for an initial wavefront direction at the source location for which the ray passes through the observer location [24,25]. This leads to similar methodologies as found in optics relating to Snell's law or Huygens principle, where either the ray or wavefront is traced through the flow. The other possibility is to solve a boundary value problem and solve the ray as the path of stationary action (or minimal acoustic delay time) [26,27], known in optics as Fermat's principle. Depending on the modelling of flow, e.g., continuous or discrete, and the exact formulation both methods

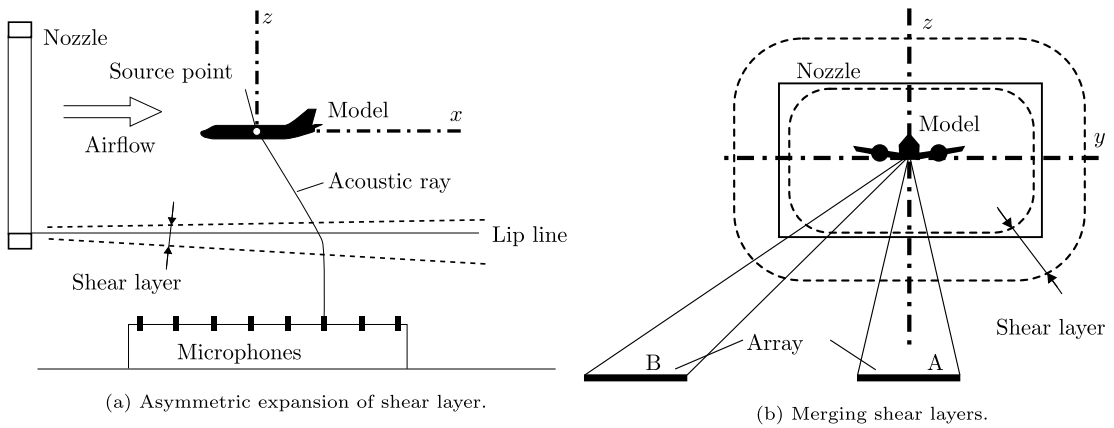

(a) Asymmetric expansion of shear layer.

(b) Merging shear layers.

Fig. 1. Typical setup for an (aero)acoustic open jet wind tunnel test.

may offer benefits over the other in terms of simpleness, computational effort or accuracy. Gottlieb [28] derived analytical solutions to compute the phase of the acoustic pressure generated by a sound source near a velocity discontinuity, specifically a vortex sheet. When the shear layer is thin and approximately planar the flow can indeed be modelled as a vortex sheet, e.g., in the correction methodology of Amiet [29,30]. The results of Amiet were confirmed by experimental work performed by Plumbee [31], Ahuja [32], and Bahr [33]. In addition to experimental work in a 0.76 m × 1.07 m wind tunnel Plumbee also performed a numerical study to assert that the influence of the shear layer thickness on the refraction angle was within 1°, and thus neglectable in the academically scaled wind tunnel. For radially symmetric shear flows, with a thin shear layer, Morfey [34] derived an analytical expression for the propagation time based on the vortex sheet assumption. Porteous [35] generalized the vortex sheet approach and derived an analytical solution for any convex vortex sheet. Porteous computed the ray paths using the least acoustic time formulation, which resulted in a computationally inexpensive methodology. The parameterization of the convex vortex sheet was independent from the wind tunnel x-coordinate. This limits the extend of the method, e.g., flow models for an expanding shear layer or displaced potential core are inherently dependent on the wind tunnel x-coordinate.

A semi-analytical solution for continuous flow with radial symmetry has been derived by Candel [36] and Tam [37]. Candel [38] also derived a similar solution for a shear layer with finite (constant) thickness. In order to reduce the computational effort of ray-tracers Sarradj [24] used a ray-casting method to compute the delay-time at a few points and interpolated the results between these points. Padois [39] compared the Amiet methodology with results obtained from solving the linearized Euler equations. The numerical predictions compared favourably with an experiment in which a loudspeaker was mounted in the wind tunnel wall. A CAA solution was presented by Redonnet [40,41] to compute the refraction effects for a planar shear layer and a radial symmetric shear layer. Casalino [42] performed a finite element method computation, presenting a discretization scheme for the Lilley–Goldstein acoustic analogy for sound propagation through a non-isothermal axial symmetric jet. Jiao [43,44] carried out combined CFD and CAA computations to study multiple propagation phenomena including: the refraction of sound by a finite shear layer, a displaced shear layer, and wavefront distortion due to the shear layer turbulence, using a synthetic turbulence method.

Observing the current state-of-the-art there is a clear spectrum of computational schemes available. One side of the spectrum is focused on detailed acoustic propagation descriptions often aided by CFD and CAA, whereas the other side aims to deliver simple and computationally inexpensive solutions at the cost of lower accuracy. The literature is consistent in the claim that the inclusion of the shear layer thickness results in small angle of arrival differences. However, inherent to the large scale of industrial wind tunnels is the presence of a thick shear layer which is combined with high accuracy standards. Combined, this means that a small error may still be relevant simply due to the large wind tunnel scale. Furthermore, realistic shear layers expand asymmetrically around the lip-line and change shape as function of the wind tunnel x-coordinate, which should be included in the flow description. Lastly, a simple mathematical description to model the merging of finite thickness shear layers has not been found in the literature.

In this paper a correction methodology for arbitrary jet flows is developed. With the methodology acoustic delay times are efficiently computed. This is mainly beneficial for beamforming codes. The methodology alleviates the need for vortex sheets and instead subdivides the velocity field into regions with an uniform velocity using velocity discontinuities. The methodology is the used to assess the effect on the acoustic propagation time for experiments in large industrial wind tunnels, with thick merging shear layers, as shown in Fig. 1. A flow model is developed that includes the shear layer thickness, the asymmetric expansion and merging of shear layers.

2. Ray-tracing with time minimization

The acoustic pressure waves are assumed to have a low amplitude [45] and a high frequency. With these assumptions the sound propagation can be modelled with the Eikonal equation [23], also known as geometrical acoustics. Within the framework

of geometrical acoustics the solution is the acoustic ray travelling from source to observer. The ray can be solved with multiple methods. In this work solutions are based upon the minimization of the acoustic propagation time, also know as Fermat's principle. Fermat's principle defines the acoustic ray trajectory as the path of least travel time between two locations. Fig. 2 shows a sound ray connecting points A and B. There are an infinite amount of rays that connect these points. However, the principle of Fermat states that the physical path is the path of least propagation time, i.e., the fastest path between A and B. The time minimization scheme offers a simple method to solve for the acoustic rays and the acoustic propagation time in the rest of the paper.

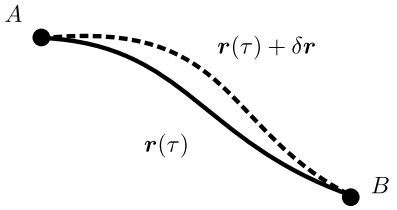

Fig. 2. Acoustic path and variational principle.

This section summarizes how Fermat's principle yields the same solution as obtained from a conventional ray-tracer for continuous velocity fields. The explanation is based on the work of Uginčius [26].

2.1. Sound propagation & sound rays

Suppose that a ray $\hat{\boldsymbol{r}}$ tracks a surface of equal phase $\hat{\boldsymbol{\Phi}}$ as function of time t while interacting with the averaged velocity field $\overline{\boldsymbol{U}}$. A reference length L and the thermodynamic speed of sound c_T, assumed constant, are used to define the following non-dimensional quantities:

$$\boldsymbol{r} = \hat{\boldsymbol{r}}/L; \qquad \boldsymbol{\Phi} = \hat{\boldsymbol{\Phi}}/L; \qquad \tau = tc_T/L; \qquad \boldsymbol{M} = \overline{\boldsymbol{U}}/c_T. \tag{1}$$

Fig. 3 shows a surface of constant non-dimensional phase $\boldsymbol{\Phi}$ (the wavefront) with normal vector $\boldsymbol{n}$. The Eikonal equation approximates the wavefront phase function in a fluid and in non-dimensional form is given as:

$$|\boldsymbol{\nabla\Phi}|^2 = |1 - \boldsymbol{M}\cdot\boldsymbol{\nabla\Phi}|^2 . \tag{2}$$

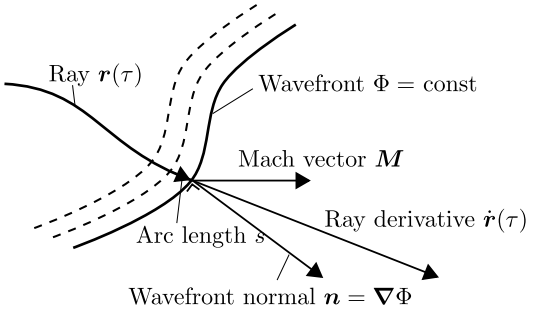

Fig. 3. Propagation of the wavefront.

Eq. (2) is a first order non-linear partial differential equation valid for acoustic waves of small amplitude. The local flow velocity is denoted by the Mach vector $\boldsymbol{M}$, the ray path $\boldsymbol{r}(\tau)$ depends on τ the equivalent time parameter. The Cauchy method of characteristics, see Evans [46](Ch 3, pg. 91), describes the transformation of a first order partial differential equation into a set of ordinary differential equations. The Eikonal equation is first written in the standard form as:

$$F(\boldsymbol{r};\boldsymbol{n};\boldsymbol{\Phi}) = |\boldsymbol{\nabla\Phi}|^2 - |1 - \boldsymbol{M}\cdot\boldsymbol{\nabla\Phi}|^2 = \boldsymbol{n}\cdot\boldsymbol{n} - (1 - \boldsymbol{M}\cdot\boldsymbol{n})^2 = 0, \tag{3}$$

where the normal vector $\boldsymbol{n} = \nabla\boldsymbol{\Phi} = \partial\boldsymbol{\Phi}/\partial\boldsymbol{r}$. The standard form defines a functional F as function of the location $\boldsymbol{r}(\tau)$, the local phase $\boldsymbol{\Phi}$ and the gradient of the phase denoted by $\boldsymbol{n}$, and F must equal zero. For the fully non-linear case the characteristics are computed according to the expressions:

$$\frac{\partial\boldsymbol{r}}{\partial\tau} = \frac{\partial F}{\partial\boldsymbol{n}}; \qquad \frac{\partial\boldsymbol{n}}{\partial\tau} = -\left[\frac{\partial F}{\partial\boldsymbol{r}} + \frac{\partial F}{\partial\boldsymbol{\Phi}}\boldsymbol{n}\right]; \qquad \frac{\partial\boldsymbol{\Phi}}{\partial\tau} = \sum_i \boldsymbol{n}_i \frac{\partial F}{\partial\boldsymbol{n}_i}. \tag{4}$$

Substituting F from Eq. (3) in Eq. (4) yields the characteristic curves parameterized by τ:

$$\frac{\partial\boldsymbol{r}}{\partial\tau} = \dot{\boldsymbol{r}} = 2\left[\boldsymbol{n} + (1 - \boldsymbol{M}\cdot\boldsymbol{n})\boldsymbol{M}\right] \tag{5}$$

$$\frac{\partial\boldsymbol{n}}{\partial\tau} = \dot{\boldsymbol{n}} = 2(1 - \boldsymbol{M}\cdot\boldsymbol{n})\left[-\boldsymbol{n}\frac{\partial\boldsymbol{M}}{\partial\boldsymbol{r}}\right]. \tag{6}$$

The modulus of $\boldsymbol{n}$ follows from Eq. (2) as:

$$|\boldsymbol{n}| = 1 - \boldsymbol{M} \cdot \boldsymbol{n}. \tag{7}$$

Eq. (7) allows to simplify Eqs. (5)–(6) into:

$$\dot{\boldsymbol{r}} = 2\left[\boldsymbol{n} + |\boldsymbol{n}|\,\boldsymbol{M}\right] \tag{8}$$

$$\dot{\boldsymbol{n}} = -2\,|\boldsymbol{n}|\,\boldsymbol{n}\frac{\partial \boldsymbol{M}}{\partial \boldsymbol{r}}, \tag{9}$$

which are 6 ordinary differential equations describing the change in ray position and the change in wavefront normal. With a given Mach vector field $\boldsymbol{M}$ the ray path is found by integrating Eqs. (8)–(9) simultaneously. The integration is often performed numerically.

2.2. Ray path equation

Eqs. (8)–(9) can also be compacted into a single equation. In this manner the resultant equation can be rewritten into one part that is explicitly changing with time and another part that is depending only on the location. The result, Eq. (16), allows to simplify the mathematics necessary to obtain Fermat's principle of acoustic propagation time minimization in Sections 2.3–2.4. Solving $\boldsymbol{n}$ from Eq. (8):

$$\boldsymbol{n} = \frac{1}{2}\dot{\boldsymbol{r}} - |\boldsymbol{n}|\,\boldsymbol{M}, \tag{10}$$

and then computing the dot product of Eq. (10) with $\boldsymbol{M}$ yields:

$$\boldsymbol{n} \cdot \boldsymbol{M} = \left[\frac{1}{2}\dot{\boldsymbol{r}} - |\boldsymbol{n}|\,\boldsymbol{M}\right] \cdot \boldsymbol{M} = 1 - |\boldsymbol{n}|\,, \tag{11}$$

from which the modulus of $\boldsymbol{n}$ is solved explicitly in terms of the ray direction and Mach vector:

$$|\boldsymbol{n}| = \frac{1 - \frac{1}{2}\dot{\boldsymbol{r}} \cdot \boldsymbol{M}}{\gamma^2}, \tag{12}$$

with the Prandtl–Glauert factor defined as:

$$\gamma^2 = 1 - |\boldsymbol{M}|^2\,. \tag{13}$$

Substituting Eq. (10) in Eq. (9) gives:

$$\frac{\partial}{\partial \tau}\left(\frac{1}{2}\dot{\boldsymbol{r}} - |\boldsymbol{n}|\,\boldsymbol{M}\right) = -2\,|\boldsymbol{n}|\,\boldsymbol{n}\frac{\partial \boldsymbol{M}}{\partial \boldsymbol{r}}. \tag{14}$$

An equation containing only the ray direction $\dot{\boldsymbol{r}}$ is obtained by rewriting Eq. (14) with the use of Eq. (10) and (12):

$$\frac{\partial}{\partial \tau}\left(\frac{1}{2}\dot{\boldsymbol{r}} - |\boldsymbol{n}|\,\boldsymbol{M}\right) = -2\frac{1 - \frac{1}{2}\dot{\boldsymbol{r}} \cdot \boldsymbol{M}}{\gamma^2}\left[\frac{1}{2}\dot{\boldsymbol{r}} - \frac{1 - \frac{1}{2}\dot{\boldsymbol{r}} \cdot \boldsymbol{M}}{\gamma^2}\boldsymbol{M}\right]\frac{\partial \boldsymbol{M}}{\partial \boldsymbol{r}} \tag{15}$$

$$\frac{\partial}{\partial \tau}\left(\frac{1}{2}\dot{\boldsymbol{r}} - \frac{1 - \frac{1}{2}\dot{\boldsymbol{r}} \cdot \boldsymbol{M}}{\gamma^2}\boldsymbol{M}\right) = \frac{\left(1 - \frac{1}{2}\dot{\boldsymbol{r}} \cdot \boldsymbol{M}\right)\gamma^2\dot{\boldsymbol{r}} - \left(1 - \frac{1}{2}\dot{\boldsymbol{r}} \cdot \boldsymbol{M}\right)^2 2\boldsymbol{M}}{\gamma^4}\frac{\partial \boldsymbol{M}}{\partial \boldsymbol{r}}. \tag{16}$$

The left hand side contains an expression whose value changes with time, whereas the expression on the right hand side is changing with position.

2.3. Lagrangian mechanics

In this section the mathematical framework of Lagrangian mechanics is used to derive a minimization problem that yields the acoustic ray path. In Lagrangian mechanics the total action is defined by the functional J as:

$$J[\boldsymbol{r}] = \int_A^B \mathcal{L}(\tau; \boldsymbol{r}; \dot{\boldsymbol{r}})\mathrm{d}\tau \tag{17}$$

Fig. 2 shows the ray path $\boldsymbol{r}$ with end points A and B. The functional J is the total action along the path. To distinguish the physical path from all possible paths between A and B a further restriction is necessary. For many physical phenomena, including the propagation of sound, the solution to the mathematical models should only depend on the boundary conditions at A and B, and not on the path between them. The true path $\boldsymbol{r}$ will then be the path of stationary action, where small changes in the path will cause no change in the total action. This condition is mathematically formulated by equating the functional derivative of the total action from Eq. (17) with respect to the change in path equal to zero:

$$\frac{\delta J[\boldsymbol{r}]}{\delta \boldsymbol{r}} = 0. \tag{18}$$

The functional derivative is denoted by δ. Eq. (18) constitutes the Euler–Lagrange (EL) equation:

$$\frac{\partial}{\partial \tau}\left(\frac{\partial \mathcal{L}}{\partial \dot{\boldsymbol{r}}}\right) = \frac{\partial \mathcal{L}}{\partial \boldsymbol{r}}. \tag{19}$$

The classical example to introduce the EL equation is to derive Newton's equation of motion from the difference between the specific kinetic energy and the specific potential energy for a point mass in a gravity potential:

$$\mathcal{L} = \underbrace{\frac{1}{2}|\dot{\boldsymbol{r}}|^2}_{\text{kinetic energy}} - \underbrace{g\,|\boldsymbol{r}|}_{\text{potential energy}} = 0. \tag{20}$$

The total specific energy is conserved, hence the difference is zero. Substituting Eq. (20) into Eq. (19) then yields:

$$\frac{\partial}{\partial \tau}(\dot{\boldsymbol{r}}) = \ddot{\boldsymbol{r}} = -g\frac{\boldsymbol{r}}{|\boldsymbol{r}|}, \tag{21}$$

i.e., the point mass is accelerating towards the centre of gravity. Since the Lagrangian is only dependent on the field variables and time it can also be applied to continuous problems. The EL equation, Eq. (19), is similar to Eq. (16) and thus the acoustic Lagrangian $\mathcal{L}$ is found by equating the left and right hand sides. Starting with the right hand side.

$$\frac{\partial \mathcal{L}}{\partial \boldsymbol{r}} = \frac{\left(1-\frac{1}{2}\dot{\boldsymbol{r}}\boldsymbol{M}\right)\gamma^2\dot{\boldsymbol{r}} - \left(1-\frac{1}{2}\dot{\boldsymbol{r}}\boldsymbol{M}\right)^2 2\boldsymbol{M}}{\gamma^4}\frac{\partial \boldsymbol{M}}{\partial \boldsymbol{r}}. \tag{22}$$

Written in this way the quotient rule for differentiation can be recognized:

$$\frac{\partial \mathcal{L}}{\partial \boldsymbol{r}} = \frac{\frac{\partial g}{\partial \boldsymbol{r}}h - \frac{\partial h}{\partial \boldsymbol{r}}g}{h^2}\frac{\partial \boldsymbol{M}}{\partial \boldsymbol{r}} = \frac{\partial}{\partial \boldsymbol{M}}\left[\frac{g(\boldsymbol{M})}{h(\boldsymbol{M})}\right]\frac{\partial \boldsymbol{M}}{\partial \boldsymbol{r}}, \tag{23}$$

where

$$h = \gamma^2 = 1 - |\boldsymbol{M}|^2; \qquad g = \left(1-\frac{1}{2}\dot{\boldsymbol{r}}\boldsymbol{M}\right)^2 \tag{24}$$

$$\frac{\partial h}{\partial \boldsymbol{M}} = 2\boldsymbol{M}; \qquad \frac{\partial g}{\partial \boldsymbol{M}} = \left(1-\frac{1}{2}\dot{\boldsymbol{r}}\boldsymbol{M}\right)\dot{\boldsymbol{r}}. \tag{25}$$

By integrating Eq. (23) it is found that:

$$\mathcal{L} = \frac{g(\boldsymbol{M})}{h(\boldsymbol{M})} + C(\dot{\boldsymbol{r}}) = \frac{\left(1-\frac{1}{2}\dot{\boldsymbol{r}}\boldsymbol{M}\right)^2}{\gamma^2} + C(\dot{\boldsymbol{r}}). \tag{26}$$

Now for the left hand sides the relevant expression becomes:

$$\frac{\partial \mathcal{L}}{\partial \dot{\boldsymbol{r}}} = \frac{\partial C}{\partial \dot{\boldsymbol{r}}} - \frac{1-\frac{1}{2}\dot{\boldsymbol{r}}\boldsymbol{M}}{\gamma^2}\boldsymbol{M}, \tag{27}$$

which yields:

$$\frac{\partial C}{\partial \dot{\boldsymbol{r}}} = \frac{1}{2}\dot{\boldsymbol{r}}. \tag{28}$$

Upon integration it is found that:

$$\mathcal{L} = \underbrace{\frac{\left(1-\frac{1}{2}\dot{\boldsymbol{r}}\cdot\boldsymbol{M}\right)^2}{\gamma^2}}_{\text{potential e.d.}} + \underbrace{\frac{1}{4}|\dot{\boldsymbol{r}}|^2}_{\text{kinetic e.d.}}. \tag{29}$$

Which is indeed equal to the Lagrangian derived by Uginčius. The acoustic energy density is split into the potential energy density and the kinetic energy density [47] (page 4, Eq. (1.6)) [48] (Eqs. (23)–(26)).

2.4. Fermat's principle

To show that the acoustic rays follow from Fermat's principle the Lagrangian from Eq. (29) is substituted into the minimization problem defined by Eq. (18). Secondly, the integration is performed with respect to the arc length s instead of the non-dimensional time parameter τ. This transform can be found in Appendix A. In the first step the Lagrangian $\mathcal{L}$ is written in terms of s such that the ray changes with respect to $\mathrm{d}s$, i.e., in terms of:

$$\boldsymbol{r}' = \frac{\partial \boldsymbol{r}}{\partial s}. \tag{30}$$

Subsequently, an expression is found that relates $\mathrm{d}\tau$ to $\mathrm{d}s$. The result is:

$$\delta J[\boldsymbol{r}] = \delta\int_A^B \mathcal{L}\,\mathrm{d}\tau = \delta\int_A^B \frac{1}{\sqrt{\gamma^2 + (\boldsymbol{r}'\cdot\boldsymbol{M})^2} + \boldsymbol{r}'\cdot\boldsymbol{M}}\mathrm{d}s = \delta\int_A^B \frac{\mathrm{d}s}{c_e} = 0. \tag{31}$$

The integrand on the right hand side of Eq. (31) is the path segment $\mathrm{d}s$ divided by an effective speed of sound equal to:

$$c_e = \left[\sqrt{\gamma^2 + (\boldsymbol{r}' \cdot \boldsymbol{M})^2} + \boldsymbol{r}' \cdot \boldsymbol{M}\right]. \tag{32}$$

More formally this is can be rewritten with the help of Eq. (18) as:

$$\frac{\delta \boldsymbol{J}[\boldsymbol{r}]}{\delta \boldsymbol{r}} = \frac{\delta \int_A^B \frac{\mathrm{d}s}{c_e}}{\delta \boldsymbol{r}} = \frac{\delta \int_A^B \mathrm{d}t}{\delta \boldsymbol{r}} = \frac{\delta T[\boldsymbol{r}]}{\delta \boldsymbol{r}} = 0, \tag{33}$$

where time infinitesimal $\mathrm{d}t$ is simply the distance infinitesimal $\mathrm{d}s$ over the effective speed of sound c_e, and T is the total propagation time. This is Fermat's principle, which states that the total propagation time integrated over the path going from A to B is the minimum propagation time. The rays obtained from a ray-tracer are thus also the rays with minimal propagation time between source and observer.

3. Ray refraction in a discretized velocity field

The previous section demonstrated that the acoustic ray follows the path that minimizes the total propagation time. This principle can be used to compute the acoustic path in complex shear flows, e.g., as shown in Fig. 4(a). The acoustic path is used to determine the source location and strength from microphone measurements. The method proposed by Amiet [29] subdivides the flow field using a vortex sheet. This works well for thin shear layers when the flow velocity in z-direction is small. When these assumptions are not valid a different approach is proposed. Fig. 4(b) shows a few isocontours for the velocity components corresponding to Fig. 4(a). The flow field is discretized into blocks in which the velocity vector is constant as illustrated in Fig. 5. The geometry of the blocks is based upon the flow topology shown in Fig. 4(b). The discretized flow should approximate the flow in the region where the acoustic rays propagate using a minimum number of blocks. The latter requirement assures a low computational cost. In Section 4.1 a continuous self-similar shear layer flow is discretized into three blocks and the interfaces are determined such that the difference between the discretized flow and the continuous flow model is minimized. The coarse discretization of the flow is used in conjunction with Fermat's principle to obtain discrete approximations of the acoustic ray. The different (non-physical) rays to optimize over are constructed by moving the interface points along the block interface as shown in Fig. 5. The angle of refraction is found implicitly by minimizing the total propagation time.

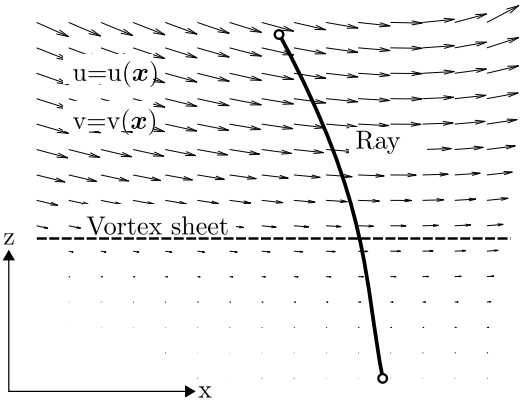

(a) Complex shear layer flow. The acoustic path is found using Fermat's principle.

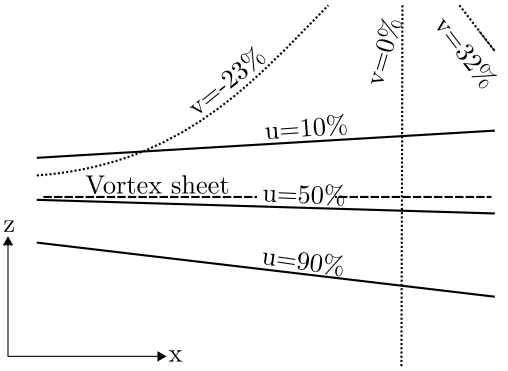

(b) Isocontours for constant horizontal (solid line) and vertical velocity (dotted line) components.

Fig. 4. Continuous velocity fields (illustrations). Vortex sheet shown for comparison.

A numerical scheme is constructed as follows: at every interface a new intersection point $(x_n; y_n)$ is created. The intersection points are then connected to form a ray. The total time T is simply the sum of all the segment lengths divided by the effective speed of sound.

$$T = \sum_{n=1}^{N} \frac{\sqrt{(x_n - x_{n-1})^2 + (y_n - y_{n-1})^2 + (z_n - z_{n-1})^2}}{c_e(\boldsymbol{x}_n; \boldsymbol{x}_{n-1}; \boldsymbol{M}_n)}. \tag{34}$$

The effective speed of sound, defined in Eq. (32), depends on the Mach vector in the block as well as the ray direction. The ray direction equals the ray segment direction. The acoustic ray path is found by changing the ray until T is minimized. For the optimal acoustic path a small change $\delta \boldsymbol{r}$ does not change T (Fermat's principle). A starting point at the source and an end point at the microphone closes the model. A note of caution is that, depending on the velocity field, caustics or reflections may be present. A caustic represents the case where acoustic rays are crossing (the solution becomes multi-valued) and the Eikonal equation is no longer valid at the caustic. Whether caustics are present depends on the specific flow discretization. Using Fermat's principle one effectively solves for the viscosity solution [49,50], i.e., one solves for the minimum acoustic time, which can always be uniquely defined given that the location can be reached by the sound wavefront.

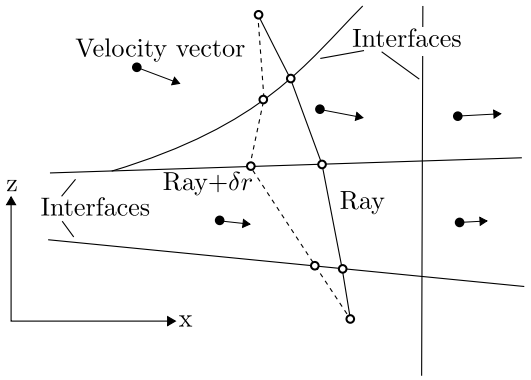

Fig. 5. Flow decomposed in blocks of uniform velocity. The acoustic ray refracts at the interfaces. Of all rays that connect the source and observer (dotted line) the physical ray (solid line) follows from Fermat's principle.

3.1. Refraction on a vortex sheet

The theory from the previous section is applied to the simple case where a vortex sheet describes the velocity field. Fig. 6 shows a vortex sheet and ray paths obtained with Fermat's principle, the Amiet theory and Snell's law (in Appendix B). This simple case allows to show that these three solutions are the same mathematical model viewed differently.

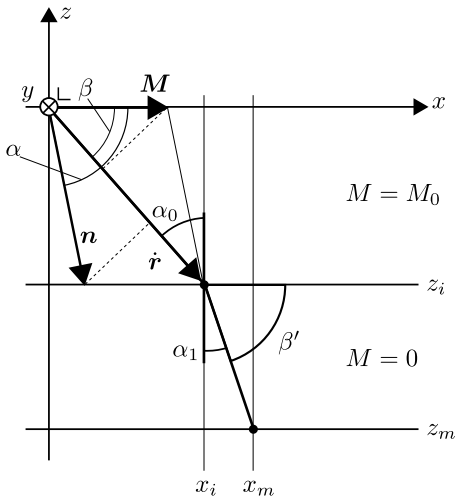

Fig. 6. Amiet, Fermat's principle and Snell's law. The y-axis points into the plane.

3.2. Fermat's principle

Starting from Fermat's principle and assuming two media with effective speeds of sound c_0 and c_1 the total travel time is computed as:

$$T = \frac{\sqrt{x_i^2 + y_i^2 + z_i^2}}{c_0} + \frac{\sqrt{(x_m - x_i)^2 + (y_m - y_i)^2 + (z_m - z_i)^2}}{c_1}, \tag{35}$$

with the effective speed of sound defined by Eq. (32). The travel time is minimized by computing the interface locations x_i and y_i that give an extremum:

$$\frac{\partial T}{\partial x_i} = \frac{x_i}{c_0\sqrt{x_i^2 + y_i^2 + z_i^2}} - \frac{\sqrt{x_i^2 + y_i^2 + z_i^2}}{c_0^2}\frac{\partial c_0}{\partial x_i} - \frac{x_m - x_i}{c_1\sqrt{(x_m - x_i)^2 + (y_m - y_i)^2 + (z_m - z_i)^2}} = 0 \tag{36}$$

$$\frac{\partial T}{\partial y_i} = \frac{y_i}{c_0\sqrt{x_i^2 + y_i^2 + z_i^2}} - \frac{\sqrt{x_i^2 + y_i^2 + z_i^2}}{c_0^2}\frac{\partial c_0}{\partial y_i} - \frac{y_m - y_i}{c_1\sqrt{(x_m - x_i)^2 + (y_m - y_i)^2 + (z_m - z_i)^2}} = 0. \tag{37}$$

3.3. Amiet

The solution to Amiet's theory as presented by Bahr [33] is found by solving two equations simultaneously:

$$f_0 = \frac{x_i}{\sqrt{x_i^2 + \gamma^2(y_i^2 + z_i^2)}} - \gamma^2 \frac{x_m - x_i}{\sqrt{(x_m - x_i)^2 + (y_m - y_i)^2 + (z_m - z_i)^2}} - M = 0 \tag{38}$$

$$f_1 = \frac{y_i}{\sqrt{x_i^2 + \gamma^2(y_i^2 + z_i^2)}} - \frac{y_m - y_i}{\sqrt{(x_m - x_i)^2 + (y_m - y_i)^2 + (z_m - z_i)^2}} = 0. \tag{39}$$

Noting the similarity between Eqs. (36)–(37) and (38)–(39) we integrate Eqs. (38)–(39) to obtain:

$$G_0 = \int \frac{f_0}{\gamma^2} \mathrm{d}x_i = \frac{\sqrt{x_i^2 + \gamma^2(y_i^2 + z_i^2)}}{\gamma^2} + \sqrt{(x_m - x_i)^2 + (y_m - y_i)^2 + (z_m - z_i)^2} - \frac{M x_i}{\gamma^2} + C_0 \tag{40}$$

$$G_1 = \int f_1 \mathrm{d}y_i = \frac{\sqrt{x_i^2 + \gamma^2(y_i^2 + z_i^2)}}{\gamma^2} + \sqrt{(x_m - x_i)^2 + (y_m - y_i)^2 + (z_m - z_i)^2} + C_1. \tag{41}$$

The integration constants C_0 and C_1 are set equal to $C_0 = 0$ and $C_1 = -M x_i/\gamma^2$ so that G_0 and G_1 are the same functions. Eqs. (38)–(39) are then simply the x_i and y_i derivatives of a single function $G = G_0 = G_1$. Rearranging the terms containing γ in Eq. (40):

$$\frac{1}{\gamma^2}\left[\sqrt{x_i^2 + \gamma^2(y_i^2 + z_i^2)} - M x_i\right] = \frac{\sqrt{x_i^2 + y_i^2 + z_i^2}}{c_0}, \tag{42}$$

where

$$c_0 = \left[\frac{x_i}{\sqrt{x_i^2 + y_i^2 + z_i^2}} M + \sqrt{\left(\frac{x_i}{\sqrt{x_i^2 + y_i^2 + z_i^2}} M\right)^2 + \gamma^2}\right]. \tag{43}$$

Comparing Eq. (42) with the first term of Eq. (35) it is found that Eq. (40) is equal to the total propagation time T from Eq. (35):

$$G = T = \frac{r_0}{c_0} + \frac{r_1}{c_1}. \tag{44}$$

The effective speed of sound c_0 in Eq. (43) equals Eq. (14) presented by Bahr [33] and equals Eq. (32) from Section 2. Thus Eqs. (38)–(38) are equal to Eqs. (36)–(37) which followed from Fermat's principle.

4. Velocity field discretization

Two particular flow fields are considered to assess the influence of the shear layer thickness, asymmetric expansion and merging shear layer as shown in Figs. 1(a)–1(b). The first step is to discretize the simple and well known self-similar shear layer proposed by Görtler [51], which describes a two-dimensional shear layer that grows linear in thickness. Velocity measurements of the shear layer are necessary to measure the two parameters in the flow model. The more complex flow in which four shear layers merge is based on modelling a changing reference contour. The reference contour is rectangular near the nozzle with increasingly rounded corners near the collector. The shortest distance to this reference contour defines the non-dimensional parameter of Görtler's shear layer model. Note that it is not the intent to accurately simulate a shear layer. The main purpose is to provide a simple velocity field description that can be discretized to predict the acoustic propagation time, as an alternative to the planar vortex sheet. Computational effort has been one of the reasons to choose the time minimization scheme, therefore, a table comparing the computational effort of the flow models and solving methods is provided in Appendix C.

4.1. Self-similar Görtler solution

The self-similar shear layer flow model as derived by Görtler [51] is equal to:

$$\frac{U(\eta)}{U_\infty} = \frac{1}{2}\left[1 + \mathrm{erf}(\eta + \eta_0)\right] \qquad \text{with} \qquad \eta = \sigma \frac{z}{x}, \tag{45}$$

where σ and η_0 are constants depending on the actual wind tunnel shear layer. σ describes the linear growth rate, whereas η_0 represents the expansion of the potential core. Plumbee [31] also used this expression, however, the variable η_0 was set constant equal to $\eta_0 = 0.297$ and in the numerical part $\sigma = 13.5$, which is a thin shear layer [52,53]. Fig. 7 shows the flow subdivided into three regions. The regions are defined by two straight lines, parameterized by b_0 and b_1. For a symmetrically expanding shear layer ($\eta_0 = 0$) b_0 and b_1 are found by solving the following integrals:

$$\int_0^{\hat{\eta}} \left|\frac{U(\eta)}{U_\infty} - \frac{1}{2}\right| \mathrm{d}\eta = \int_{\hat{\eta}}^{\infty} \left|\frac{U(\eta)}{U_\infty} - 1\right| \mathrm{d}\eta, \tag{46}$$

for $\hat{\eta}$. The integrals equal the difference in velocity between the discretized model and the continuous velocity flow while taking into account the symmetry of the error function. A value of $\hat{\eta} \approx 0.6$ solves Eq. (46), which corresponds to a velocity thickness of 80% with respect to the freestream velocity. For the case $\eta_0 \neq 0$ the mean shear layer slope is simply added to b_0 and b_1. Modelling the shear layer geometry in this manner differs from, e.g., the approach of Candel [38], who assumed the interfaces parallel to the flow direction. The numerical model is compared to the solution from Amiet who used a vortex sheet to model the velocity field. Furthermore, a ray-tracing code is used to compare the discretized results against the continuous flow model. One set of observers is at $y/L = 0$ under the source located at $(x = 1; y = 0; z = 0)/L$. A second set of observers is located offset from the wind tunnel axis at $y/L = 1.3$. With σ approaching infinity and η_0 equal to 0 the Görtler solution reduces to a vortex sheet. The results presented in Fig. 8 show that for this case the results equal the results computed with the Amiet method (see Section 3.3). The results are made non-dimensional using the propagation time without any flow effects, i.e., the results are divided by r/c.

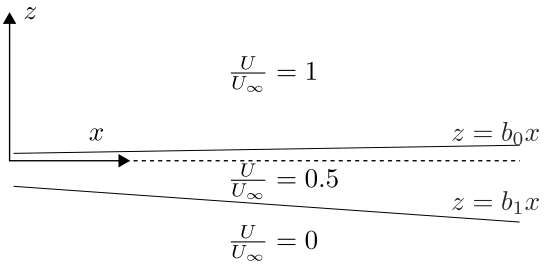

Fig. 7. Flow regions for the Görtler flow.

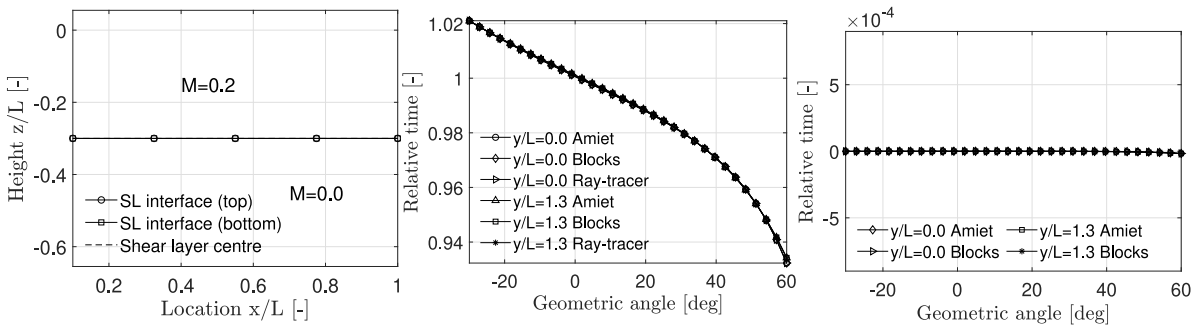

(a) Flow regions. (b) Acoustic delay time. (c) Acoustic delay w.r.t. the ray-tracer.

Fig. 8. Görtler flow parameters: $\sigma \to \infty; \eta_0 = 0$.

Increasing the complexity by adding a shear layer that grows in thickness the value for σ is set to 9. The increase in shear layer thickness causes the acoustic delay time computed with the discretized flow model to differ from the results of Amiet, this relative time difference is shown in Fig. 9. The largest difference with Amiet's method is observed downstream, this is where the shear layer is thickest. The discretized model shows the same trend as the ray-tracer demonstrating an increase in accuracy. Most shear layers tend to expand asymmetrically with respect to the nozzle lip-line. This is accomplished by setting η_0 equal to 0.31. Fig. 10 shows the numerical results obtained from these settings. Comparing with Fig. 9 it is noted that the displacement of the shear layer is an order of magnitude more of influence than the shear layer thickness.

4.2. Cross-section of the jet potential core

The two-dimensional shear layer assumption is only valid if the acoustic rays go through a two-dimensional shear layer, see e.g., array A in Fig. 1(b). The four shear layers, originating from the nozzle edge, will grow in thickness and start merging. This creates a flow that may no longer be regarded as two-dimensional since the velocity profiles in the corners are expected to blend into each other due to the growing shear layer thickness. This is modelled with an empirical model using a reference contour that changes as function of the x-coordinate. The reference contour equals the lip-line at the nozzle and changes shape when moving downstream. The reference contour is modelled by the expression:

$$\sqrt{\left|\frac{y}{W}\right|^{2/p} + \left|\frac{z}{H}\right|^{2/p}} = \text{const}, \tag{47}$$

where p is a parameter that controls the shear layer merging (velocity contour rounding), and y and z are coordinates located in a plane at a specific x location. The constants W and H are scaling parameters dependent on the wind tunnel nozzle dimensions, half the width and height respectively. Fig. 11(a) shows that varying the value of p smoothly as function of the downstream coordinate allows the curves to span a smooth surface. For small values of p the shape is approximately rectangular, e.g., near the nozzle, while

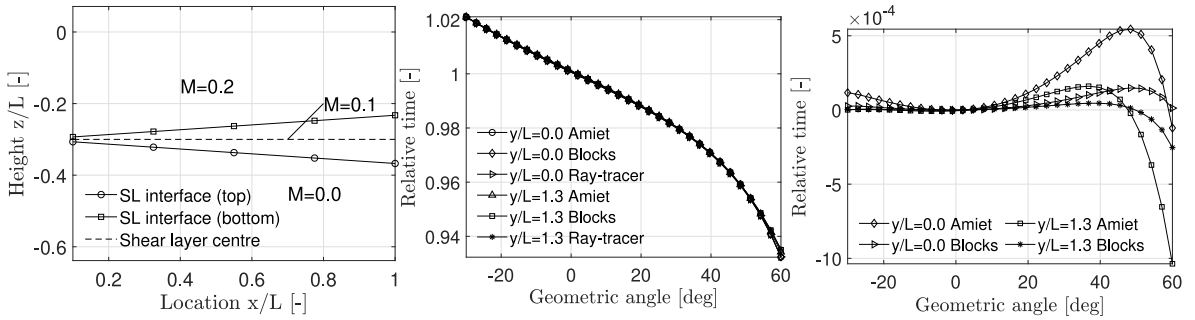

(a) Flow regions. (b) Acoustic delay time. (c) Acoustic delay w.r.t. the ray-tracer.

Fig. 9. Görtler flow parameters: $\sigma = 9; \eta_0 = 0$.

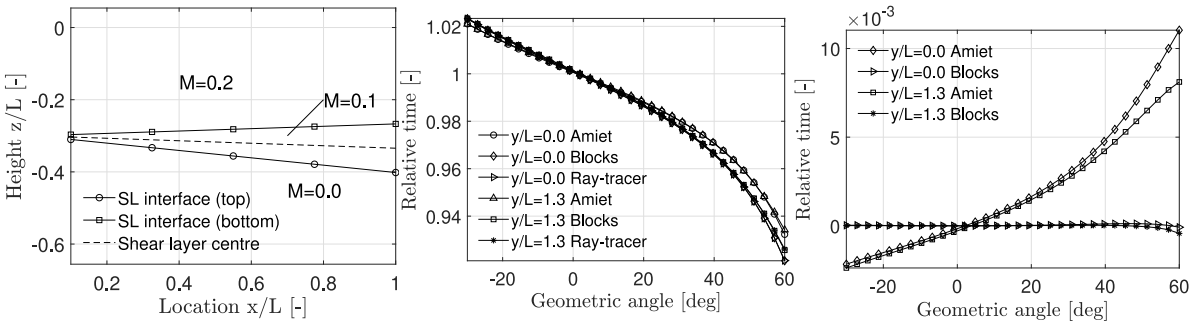

(a) Flow regions. (b) Acoustic delay time. (c) Acoustic delay w.r.t. the ray-tracer.

Fig. 10. Görtler flow parameters: $\sigma = 9; \eta_0 = 0.31$.

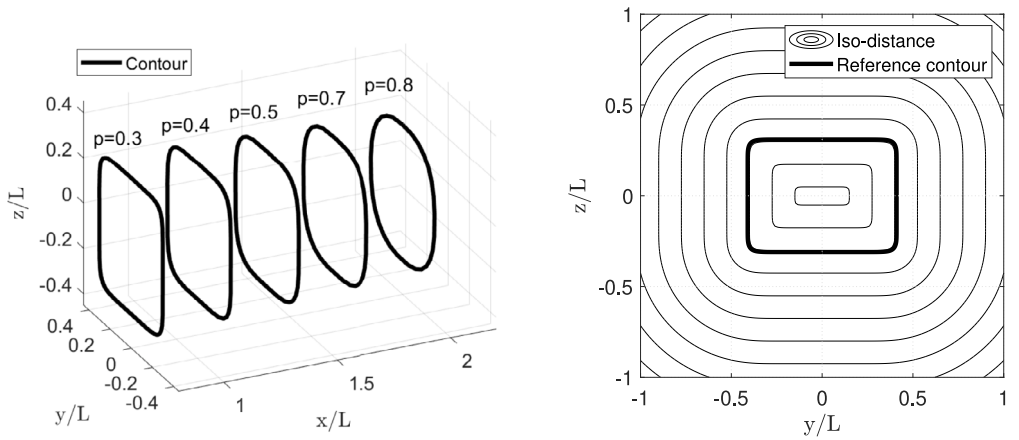

(a) Reference contours. (b) Distance to the reference contour d.

Fig. 11. Merging shear layer flow model.

for $p = 1$ the shape is an ellipse. A distance d is now defined as the shortest distance to the reference contour. Fig. 11(b) shows iso-lines for the distance d with a particular reference contour.

The shortest distance d is then used as the z coordinate in the self-similar solution (compare Eq. (45)):

$$\eta = \sigma \frac{d}{x}. \tag{48}$$

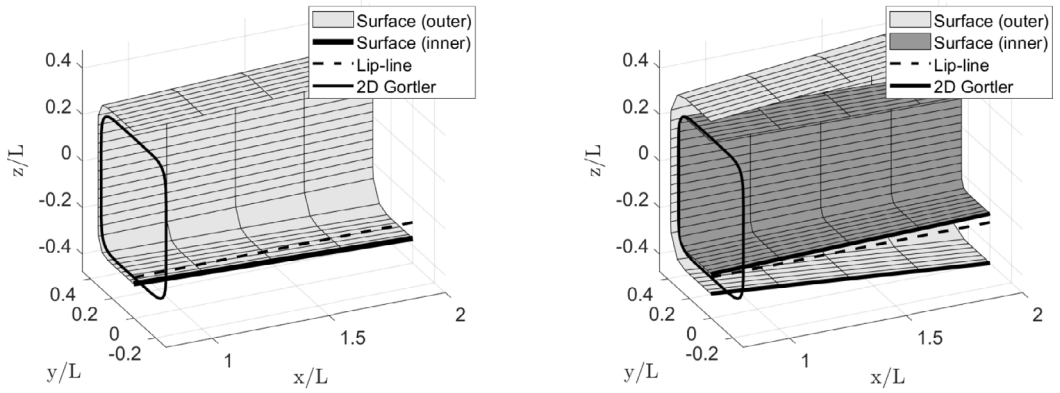

(a) 1 surface. No shear layer thickness.

(b) 2 surfaces. Thick shear layers.

Fig. 12. Regions of constant velocity. Discretization of the merging shear layer model. $\sigma = 9; \eta_0 = 0.31$.

The definition of η in Eq. (48) is similar to the two-dimensional self-similar flow definition. However, as the shear layer thickness grows it allows for the velocity contours to be curved. The reference contour (where $d = 0$) can be parameterized explicitly by a non-dimensional distance from the nozzle s with range $[0; 1]$ and the in-plane tangential parameter t with range $[0; 2\pi]$. Using $y = \sin t$ and $z = \cos t$ the definition of the contour in Eq. (47) is rewritten as:

$$S_x = Ls \qquad S_y = W \,\mathrm{sign}(\sin t)\,|\sin t|^p \qquad S_z = H \,\mathrm{sign}(\cos t)\,|\cos t|^p\,, \tag{49}$$

where $\boldsymbol{S}(s,t)$ is the surface and L is the characteristic wind tunnel length. This formulation is more convenient if the flow is to be subdivided into regions of constant velocity. Fig. 12 shows the resulting interfaces after discretizing the velocity field. The expression for p should reflect the actual wind tunnel velocity profiles. One may chose p equal to:

$$p(s) = \frac{a_0 s^2 + 2a_1 s + 1}{2a_2}, \tag{50}$$

which yields a smooth surface $\boldsymbol{S}(s,t)$. For practical applications the a_i are fitted to velocity profiles obtained from experiments, e.g., with a Pitot-static tube as performed by Biesheuvel [54]. The work also provides a numerically robust manner of describing S_y and S_z in Appendices A and B.

Fig. 13 shows acoustic delay times obtained by letting σ approach infinity and setting η_0 equal to 0. Below the wind tunnel axis this setup is effectively equal to Amiet. Since the vortex sheet does not depend on the x-coordinate the approach is equal to that of Porteous [35], with the shape of the convex vortex sheet defined by Eq. (49). The largest difference with respect to Amiet is found when the observers are placed offset from the wind tunnel axis and the acoustic rays travel through a curved shear layer. Modelling the linear growth of the shear layer by setting σ equal to 9 gives results as shown in Fig. 14. The results at $y/L = 0$ equal the two-dimensional shear layer approach. The results at $y/L = 1.3$ are now representing the influence of both the finite thickness as well as the merging of the shear layers. Setting $\eta_0 = 0.31$, as in Fig. 15, the numerical results now include all three effects; finite thickness, asymmetric shear layer expansion and merging. The differences due to the asymmetric expansion and merging are of the same order. The asymmetric expansion increases the acoustic delay, whereas the merging effect decreases the acoustic delay, and partly cancel each other.

5. Experimental results

This section first describes the validation of the simplified flow model that describes the shear layer merging. For practical reasons these measurements are performed in an academically scaled wind tunnel. The effect of the merging shear layers, as presented in Fig. 1, on acoustic images is subsequently assessed for an industrial scale facility. In the latter test a custom speaker source was placed in the wind tunnel.

5.1. Anechoic wind tunnel with an open jet test section

Experiments performed in the Anechoic Wind Tunnel (NLR-AWT) of the Royal Netherlands Aerospace Centre support the validation of the flow model presented in this paper. The nozzle dimensions are 0.95×0.95 m^2. The velocity profile in the shear layer flow is mapped by a Pitot-static tube traversing multiple sections of the wind tunnel. Subsequently, the interaction of the four shear layers originating from the nozzle is analysed. Fig. 16(a) shows the measured velocity profile of the shear layer. Results were obtained for Mach numbers $M_\infty = 0.12$ and $M_\infty = 0.17$ at 0.5, 1.25, 2.0 and 2.75 m downstream from the nozzle. The self-similar parameters are listed in Table 1 and computed by fitting the velocity field model to the measured shear layer profiles. On a course

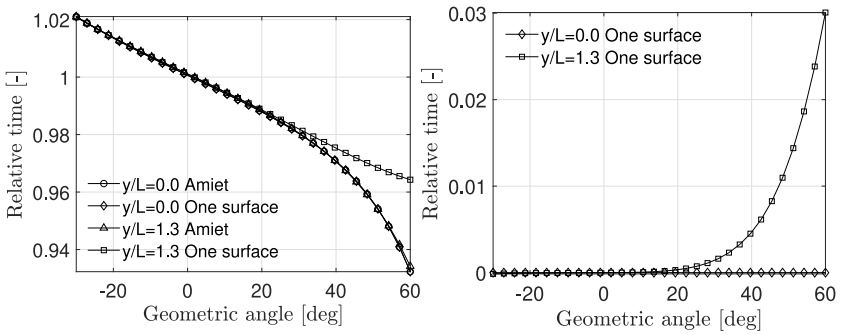

(a) Acoustic delay time. (b) Acoustic delay w.r.t. Amiet.

Fig. 13. Görtler flow parameters: $\sigma \to \infty; \eta_0 = 0$.

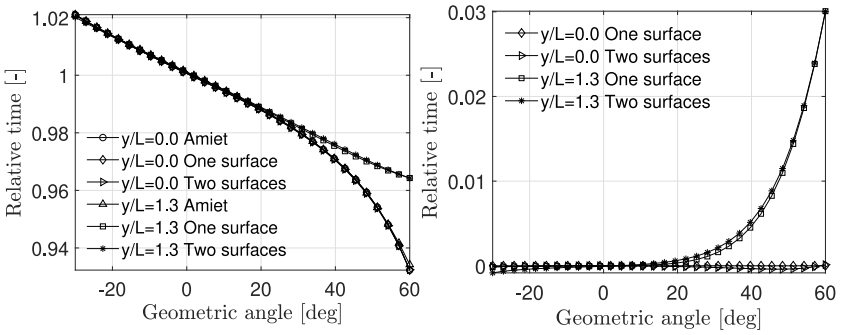

(a) Acoustic delay time. (b) Acoustic delay w.r.t. Amiet.

Fig. 14. Görtler flow parameters: $\sigma = 9; \eta_0 = 0$.

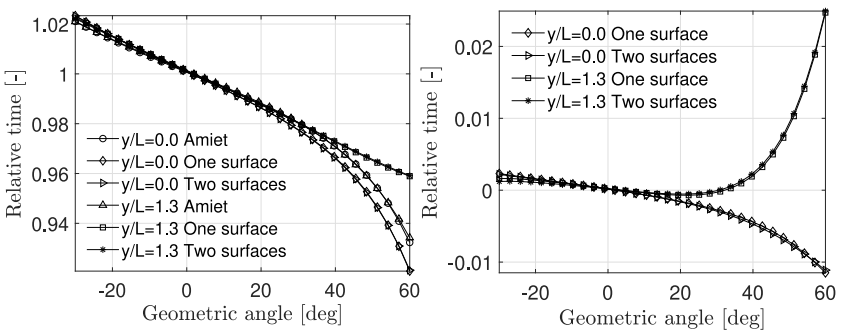

(a) Acoustic delay time. (b) Acoustic delay w.r.t. Amiet.

Fig. 15. Görtler flow parameters: $\sigma = 9; \eta_0 = 0.31$.

grid the flow was scanned with the Pitot-static tube for Mach number $M_\infty = 0.12$. This measurement is performed at the same 4 downstream locations. Resulting flow contours are shown in Fig. 17. For each section the optimal value of p is found that minimizes the difference between the model velocity and the experimental velocity field. The results showed that the effective width W and height H are not identical to the geometrical width and height of the nozzle. Following, Eq. (50) is fitted to the optimal p values shown in Fig. 16(b).

Fig. 17 also shows the velocity distribution produced by the fitted model. It is observed that for this wind tunnel the rounding of the velocity contours is mainly due to the spreading of the shear layer and the iso-contours as described in Fig. 11(a) remain mostly square. The resulting coefficients are listed in Table 1. The Pearson's correlation coefficient between the merging shear layer flow model and the experimentally measured velocity distribution was 0.98.

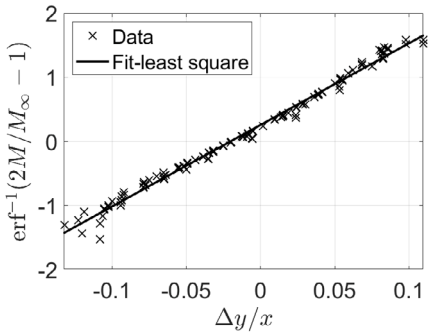

(a) Self-similar shear layer, measured and linear least square fit.

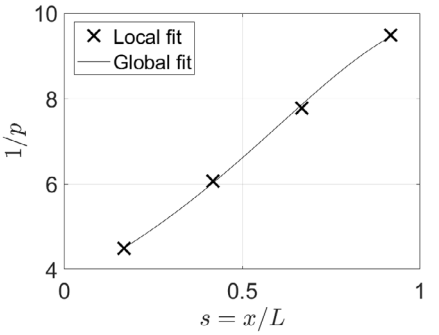

(b) Inverse power $(1/p)$, as found in Eq. 47. Per plane best fit and global best fit as in Eq. 50.

Fig. 16. Flow model parameter fit.

Table 1
Parameters for the NLR AWT.

Parameter	Value	Parameter	Value
σ	12.7	η_0	0.258
a_0	−0.350	a_1	0.0669
a_2	4.350	W	0.475 m
H	0.515 m	L	3 m

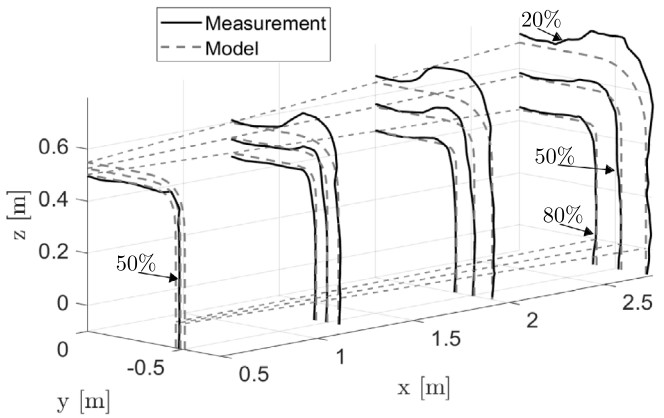

Fig. 17. Flow velocity in NLR's Anechoic Wind Tunnel, measured with a Pitot-static tube.

5.2. Speaker in a large-low velocity facility

A large scale wind tunnel test was performed in the DNW-LLF wind tunnel with a test section of 8 × 6 m^2 to demonstrate the applicability of the correction methodology and assess the effects of shear layer thickness, asymmetric expansion and shear layer merging. The measurement setup can be seen in Fig. 18. A custom speaker source has been placed near the centre of the test section of the wind tunnel instead of an aircraft model as in Fig. 1.

Fig. 18(b) shows the speaker source consisting out of an aluminum shell with 3 actual loudspeakers. The loudspeakers face in the −30°, 0° and +30° direction relative to the negative z-axis. For each loudspeaker the input signal was controlled independently. The geometric source location was determined using a theodolite. With the geometric location a beamforming grid was defined. Subsequently, the reference source location was determined using beamforming and a measurement with the wind tunnel turned off. A small difference of 2.5 cm between the geometric location of the source and the beamforming location was found in the x-direction. This difference was the identical for all loudspeakers. The speaker source was driven with a broadband white noise signal filtered to the range of 5 kHz to 20 kHz. Acoustics measurements were done with an out-of-flow microphone array. The acoustic array (4 × 4 m^2) contained 140 microphones sampled at a rate of 65 kHz (for a schematic representation see Fig. 18(a)). The acquisition time was 45 s per data point. The array was traversable over a distance of −4 m to +4 m. The exact position of the array with respect to the wind tunnel reference is known with a precision of a few centimeters by use of a theodolite. The

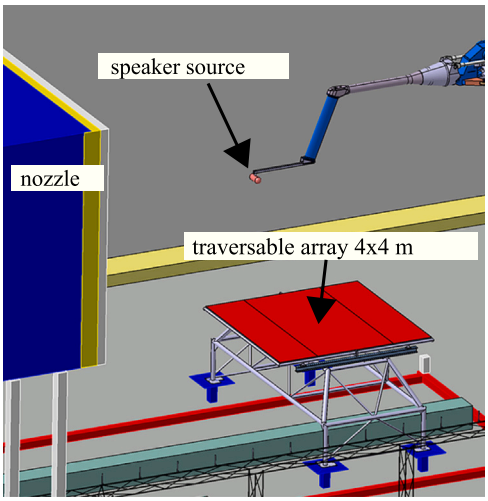

(a) Wind tunnel setup (all to scale).

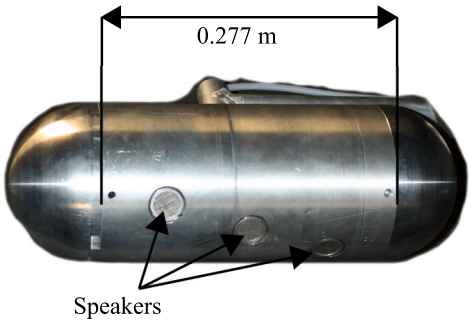

(b) Custom sound source. Made from alluminium shell with 3 BMS 4540ND Drivers installed. Each speaker delivers up to 132 dB SPL.

Fig. 18. Wind tunnel experiment hardware.

Table 2
Parameters for the 1:10 scaled DNW-LLF.

Parameter	Value	Parameter	Value
σ	12.6	η_0	0.407
a_0	−5.14	a_1	5.31
a_2	10.3	W	0.4 m
H	0.3 m	L	2 m

parameters σ, η_0, and the coefficients in Eq. (50) are based on Pitot-static measurements obtained in a 1:10 scale wind tunnel of the DNW-LLF. The numerical values are given in Table 2. The Pearson's correlation coefficient between the merging shear layer flow model and the experimentally measured velocity distribution was 0.99. Fig. 19 summarizes the beamforming results for the experiment. The beamforming process used data blocks of 4096 samples. The 5 kHz band is used for the beamforming process. The array was positioned at three positions: at −4 m, 0 m, and +4 m with respect to the wind tunnel centre. For all three measurements the loudspeaker directed downstream was used. The steering vector used for the beamforming is based on the propagation time correction. This definition ensures that the location of maximum SPL coincides with the source location [55] (formulation I). Since a pressure correction is not included in the steering vector the relative source power is presented. The acoustic propagation time is computed using Amiet (a) and the method presented, including the effects of expanding merging shear layers. The two-dimensional flow is discretized into 3 regions (b). The three-dimensional flow (with shear layer merging) is discretized into 2 regions (c) and 3 regions (d).

It is observed that for the array measurements at −4 m and 0 m the methods offer similar results, with the maximum beamformed source power sufficiently close to the reference location. For the array measurement at +4 m the, the processed results with steering vectors based on Amiet's method show a clear difference between the maximum beamformed source power and the reference location. The difference decreases by 3 cm when the shear layer thickness is included. Including the shear layer merging in (c) and (d) shows the maximum beamforming response moving 6 cm closer to the reference location compare to Amiet. When the array is at +4 m the acoustic rays travel through a shear layer that is sufficiently different from the vortex sheet as modelled by Amiet to be noticeable. The difference due to shear layer thickness appears to be neglectable. A small difference can be attributed to the asymmetric expansion and the merging of the shear layers. Furthermore, it is noted that the thick shear layer does not only change the time-invariant wavefront propagation but also the time-dependent wavefront propagation. The interaction of the wavefront with turbulence creates blurred acoustic images due to a loss of microphone signal coherence. This creates further uncertainty on the true source location.

6. Conclusion

A method based on the discretization of the velocity vector field and acoustic time delay minimization is presented. This method extends the range of experimental configurations for which acoustic time-delays can be computed compared to the current state-of-the-art. Furthermore, it is able to predict the significance of flow characteristics on the acoustics corrections, e.g., the effects of shear layer thickness and the merging of shear layers. Sound rays are efficiently computed by minimizing the travel time between source

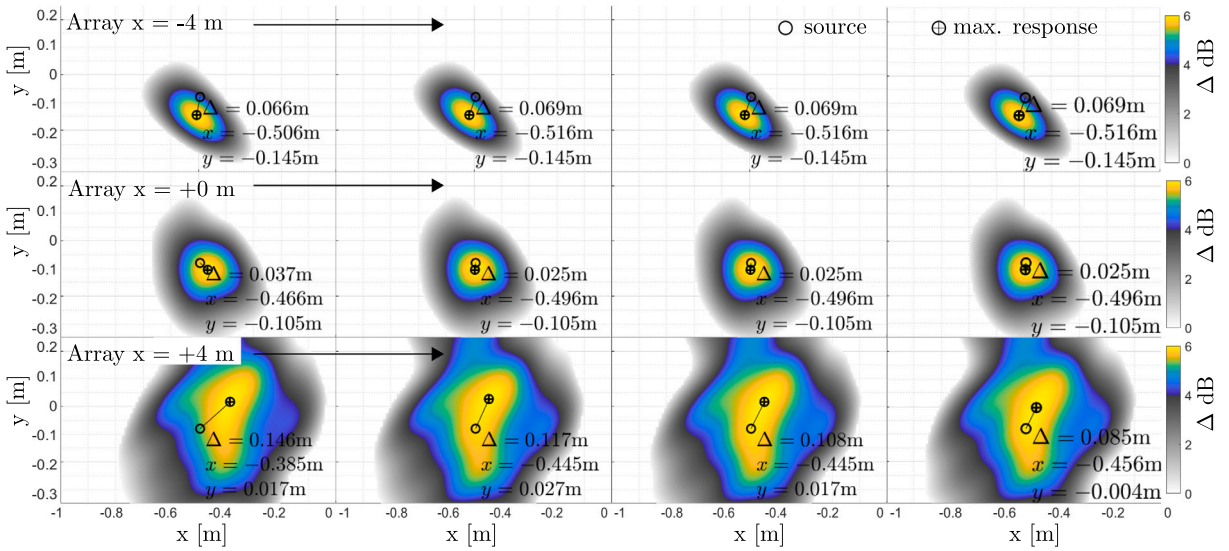

Fig. 19. Conventional beamforming with different acoustic delay prediction models for different array locations. Frequency of interest is 5 kHz.

and observer. The proposed approach is equal to Amiet's theory for the baseline condition of a flow approximated by a flat vortex sheet. However, the novel method allows the acoustic rays to be computed for complex flow fields which cannot be approximated by a vortex sheet. The proposed method is fast when compared to ray-tracers and requires similar computation time as Amiet's approach.

Two flow fields commonly encountered in wind tunnels were elaborated. The first represents the finite thickness shear layer and the second a three-dimensional flow that captures the effects of merging shear layers. Pitot-static tube measurements showed that both models adequately represent the flow in an open jet wind tunnel. The solutions produced from Fermat's principle are compared with the numerical ray-traced solutions. The differences in acoustic delay-time compared with Amiet's method are in general small for the wind tunnel parameters adopted in the numerical comparison. The main differences are found when the shear layer location deviates from the flat vortex sheet. Sound source localization inaccuracies arise mainly due to the asymmetric expansion and shear layer merging. An experiment performed in a large industrial wind tunnel, with a nozzle of 8×6 m^2, showed that including the finite thickness and rounding shear layer increases the accuracy. This improved the localization accuracy by 6 cm.

Funding sources

This research was developed in the context of the Silent Approach project receiving partial funding from the Top Technology Twente program (Netherlands) in the framework of the TKI-HTSM roadmap Aeronautics.

CRediT authorship contribution statement

J. Biesheuvel: Writing the paper/researching. **M. Tuinstra:** Writing/researching, Funding acquisition. **L.D. de Santana:** Writing/researching, Funding acquisition. **C.H. Venner:** Writing/researching, Funding acquisition.

Declaration of competing interest

The authors declare that they have no known competing financial interests or personal relationships that could have appeared to influence the work reported in this paper.

Data availability

The data that has been used is confidential.

Acknowledgements

The authors are grateful to Royal Netherlands Aerospace Centre (NLR), particularly Mr. Cornelissen for his expertise in wind tunnel testing. We want to express our gratitude to the German-Dutch Wind tunnels (DNW) for making available the DNW-LLF facility for this research and development of the speaker source. In particular we want to thank Mr. Holthusen for his support. The efforts of Embraer and their employees supporting this investigation are also appreciated.

Appendix A. Ray-tracing: Tracing with time or arc length

Instead of the canonical parameter τ, the arc length s can be used to trace the ray:

$$\frac{\partial \boldsymbol{r}}{\partial \tau} = \frac{\partial \boldsymbol{r}}{\partial s}\frac{\mathrm{d}s}{\mathrm{d}\tau} = \boldsymbol{r}'\frac{\mathrm{d}s}{\mathrm{d}\tau}. \tag{A.1}$$

To derive $\mathrm{d}\tau/\mathrm{d}s$ Eq. (A.1) is substituted into Eq. (10):

$$\boldsymbol{n} = \frac{1}{2}\boldsymbol{r}'\frac{\mathrm{d}s}{\mathrm{d}\tau} - |\boldsymbol{n}|\,\boldsymbol{M}, \tag{A.2}$$

and squaring the result yields:

$$|\boldsymbol{n}|^2 = \frac{1}{4}|\boldsymbol{r}'|^2\left|\frac{\mathrm{d}s}{d\tau}\right|^2 - \boldsymbol{r}'\cdot\frac{\mathrm{d}s}{d\tau}|\boldsymbol{n}|\,\boldsymbol{M} + |\boldsymbol{n}|^2|\boldsymbol{M}|^2. \tag{A.3}$$

Since $\boldsymbol{r}'$ is the unit vector tangent to the ray one may use $|\boldsymbol{r}'| = 1$, which allows to rewrite Eq. (A.3) to:

$$\frac{1}{4}\left|\frac{\mathrm{d}s}{\mathrm{d}\tau}\right|^2 = |\boldsymbol{n}|\left[|\boldsymbol{n}|\gamma^2 + \boldsymbol{r}'\cdot\frac{\mathrm{d}s}{\mathrm{d}\tau}\boldsymbol{M}\right] = \left(\frac{1-\frac{1}{2}\boldsymbol{r}'\cdot\frac{\mathrm{d}s}{\mathrm{d}\tau}\boldsymbol{M}}{\gamma^2}\right)\left[1+\frac{1}{2}\boldsymbol{r}'\cdot\frac{\mathrm{d}s}{\mathrm{d}\tau}\boldsymbol{M}\right] = \frac{1-\frac{1}{4}\left(\boldsymbol{r}'\cdot\frac{\mathrm{d}s}{\mathrm{d}\tau}\boldsymbol{M}\right)^2}{\gamma^2}, \tag{A.4}$$

and finally yields an expression which can be solved for $\mathrm{d}s/\mathrm{d}\tau$:

$$\frac{1}{4}\left|\frac{\mathrm{d}s}{\mathrm{d}\tau}\right|^2\left[\gamma^2 + \left(\boldsymbol{r}'\cdot\boldsymbol{M}\right)^2\right] = 1, \tag{A.5}$$

from which the modulus follows as:

$$\left|\frac{\mathrm{d}s}{\mathrm{d}\tau}\right| = \frac{2}{\sqrt{\gamma^2 + (\boldsymbol{r}'\cdot\boldsymbol{M})^2}} = \frac{2}{S}. \tag{A.6}$$

Similarly the modulus of the scaled wave front normal $\boldsymbol{n}$ is computed from Eqs. (12) and (A.6):

$$|\boldsymbol{n}| = \frac{1-\frac{1}{2}\dot{\boldsymbol{r}}\cdot\boldsymbol{M}}{\gamma^2} = \frac{1-\frac{\boldsymbol{r}'}{S}\cdot\boldsymbol{M}}{\gamma^2} = \frac{S^2 - \boldsymbol{r}'\cdot S\boldsymbol{M}}{S^2\gamma^2} \tag{A.7}$$

$$= \frac{(S+\boldsymbol{r}'\cdot\boldsymbol{M})(S-\boldsymbol{r}'\cdot\boldsymbol{M})}{(S+\boldsymbol{r}'\cdot\boldsymbol{M})S\gamma^2} = \frac{S^2-(\boldsymbol{r}'\cdot\boldsymbol{M})^2}{(S+\boldsymbol{r}'\cdot\boldsymbol{M})S\gamma^2} = \frac{1}{S(S+\boldsymbol{r}'\cdot\boldsymbol{M})}. \tag{A.8}$$

A useful expression to introduce is:

$$\boldsymbol{r}'\cdot\boldsymbol{M}S = \boldsymbol{r}'\cdot\boldsymbol{M}\sqrt{\gamma^2 + (\boldsymbol{r}'\cdot\boldsymbol{M})^2} = \sqrt{\gamma^2|\boldsymbol{r}'|^2|\boldsymbol{M}|^2 + |\boldsymbol{r}'|^4|\boldsymbol{M}|^4} = 1. \tag{A.9}$$

Replacing the canonical parameter τ with the arc length s results in:

$$\mathcal{L}(s) = \frac{1}{S^2} + \frac{\left(1-\frac{\boldsymbol{r}'}{S}\cdot\boldsymbol{M}\right)^2}{\gamma^2} = \frac{\gamma^2 + \left(\boldsymbol{r}'\cdot\boldsymbol{M}\right)^2 - 2\boldsymbol{r}'\cdot\boldsymbol{M}S}{S^2\gamma^2} = \frac{2S(S-\boldsymbol{r}'\cdot\boldsymbol{M})}{S^2\gamma^2} = 2|\boldsymbol{n}|(s), \tag{A.10}$$

and finally:

$$\delta\int\mathcal{L}\mathrm{d}\tau = \delta\int 2|\boldsymbol{n}|\frac{\mathrm{d}\tau}{\mathrm{d}s}\mathrm{d}s = \delta\int|\boldsymbol{n}|S\mathrm{d}s = \delta\int\frac{1}{S+\boldsymbol{r}'\cdot\boldsymbol{M}}\mathrm{d}s = \delta\int_A^B\frac{\mathrm{d}s}{c_e} = 0. \tag{A.11}$$

Appendix B. Snell's law

Eq. (35) permits to derive Snell's law from Fermat's principle. Starting with Eq. (A3) from Amiet [29]:

$$\cos\beta' = \frac{1}{\gamma^2}\left[\frac{\cos\beta}{\sqrt{\cos^2\beta M^2 + 1 - M^2}} - M\right] = \frac{1}{\gamma^2}\left[\frac{\frac{x}{\sqrt{x^2+z^2}}}{\sqrt{\frac{x^2}{x^2+z^2}M^2 + 1 - M^2}} - M\right] \tag{B.1}$$

$$= \frac{1}{\gamma^2}\left[\frac{x}{\sqrt{x^2M^2(x^2+z^2)(1-M^2)}} - M\right] = \frac{1}{\gamma^2}\left[\frac{x}{\sqrt{x^2+\gamma^2z^2}} - M\right] \tag{B.2}$$

and using the "inflow" part of Eq. (35) differentiation with respect to x yields:

$$\frac{\partial}{\partial x}\left[\frac{\sqrt{x^2+z^2}}{c_0}\right] = \frac{\partial}{\partial x}\left[\frac{1}{\gamma^2}\left[Mx - \sqrt{x^2+\gamma^2z^2}\right]\right] = \frac{1}{\gamma^2}\left[M - \frac{x}{\sqrt{x^2+\gamma^2z^2}}\right] \tag{B.3}$$

The "outflow" part is written as:

$$\frac{x_m - x}{\sqrt{(x_m-x)^2 + (z_m-z)^2}} = \sin\alpha_1 \tag{B.4}$$

Combining Eqs. (B.2)–(B.4) yields:

$$\underbrace{\frac{1}{\gamma^2}\left[\frac{1}{\sqrt{\sin\alpha_0^2 M^2 + 1 - M^2}} - \frac{M}{\sin\alpha_0}\right]}_{n_0} \sin\alpha_0 = n_1 \sin\alpha_1 \tag{B.5}$$

where n_0 is the effective refractive index in the flow and $n_1 = 1$ the refractive index out of the flow. This expression represents the connection with Snell's law. In case of waves propagation through the atmosphere multiple and similar approaches for computing refraction are summarized by Ostashev [56] with Eq. (B.5) equal to Eq. (3) from the appendix of Hohenwarter [57].

Appendix C. Performance comparisons

Our implementation is written entirely in C++. The computational effort of the methods discussed in this paper are shown in Table C.3. The equations of Amiet, i.e., Eqs. (38)–(39), are solved using 10 steps of a Newton–Raphson solver which brings the residual under $4 \cdot 10^{-16}$. The ray-tracer numerically integrates Eqs. (8)–(9) using an adaptive integration scheme [58]. The time step is set to $2 \cdot 10^{-6}$ s. A minimization method is used to solve for the initial ray direction such that the ray goes through the observer location within a tolerance of 0.3 mm. A number of "trial-rays" are followed in order to find the correct ray connecting the two points. The minimization method used is the Nelder–Mead algorithm [59] which on average shoots 220 trial-rays to obtain the correct ray. The propagation time minimization method (Fermat's principle) uses the same Nelder–Mead minimization method with a error criterion set to $2 \cdot 10^{-6}$ s. For the Fermat case with 1 surface an average of 84 trial-rays are necessary to find the physical acoustic path. When two surfaces are used an average of 260 trial-rays are used.

The Amiet method and the Fermat solving methods are similar in computational effort. The Fermat 3D vortex sheet is slower than Amiet due to the need to compute the exponential in Eq. (49). Furthermore, the Fermat 3D shear layer is slowed down by the need to solve 4 unknowns. The ray-tracer is much slower since the flow field must be evaluated at each step of the ray-tracer. The 3D flow field significantly slows down the computation, the solver evaluates the flow field multiple times at each step in order to numerically approximate the derivatives of Eq. (48) to subsequently obtain the velocity derivatives using the chain rule of differentiation.

Table C.3
Computational effort. A ray is the solution between two points A and B. Multiple "trial-rays" are traced from point A to obtain the ray that intersects with point B.

Solver	Flow type	CPU seconds/1000 rays	CPU seconds/1000 trial-rays
Amiet	Vortex sheet	0.0089	$8.9{\cdot}10^{-4}$
Raytracer	2D shear layer	222	0.96
Raytracer	3D shear layer	3506	16
Fermat	2D shear layer	0.040	$1.5{\cdot}10^{-4}$
Fermat	3D vortex sheet	0.044	$5.3{\cdot}10^{-4}$
Fermat	3D shear layer	0.25	$9.7{\cdot}10^{-4}$

References

[1] H. Holthusen, A. Bergmann, P. Sijtsma, Investigations and measures to improve the acoustic characteristics of the German-Dutch wind tunnel DNW-LLF, in: 18th AIAA/CEAS Aeroacoustics Conference (33rd AIAA Aeroacoustics Conference), American Institute of Aeronautics and Astronautics, 2012, http://dx.doi.org/10.2514/6.2012-2176.

[2] L.D. de Santana, M.P. Sanders, C.H. Venner, H.W. Hoeijmakers, The UTwente aeroacoustic wind tunnel upgrade, in: 2018 AIAA/CEAS Aeroacoustics Conference Session: Advanced Testing Techniques III, American Institute of Aeronautics and Astronautics, 2018, http://dx.doi.org/10.2514/6.2018-3136.

[3] A. Finez, M. Jacob, E. Jondeau, M. Roger, Broadband noise reduction with trailing edge brushes, in: 16th AIAA/CEAS Aeroacoustics Conference, American Institute of Aeronautics and Astronautics, 2010, http://dx.doi.org/10.2514/6.2010-3980.

[4] S. Oerlemans, Detection of Aeroacoustic Sound Sources on Aircraft and Wind Turbines (Ph.D. thesis), Universiteit Twente, 2009.

[5] J.P. Gomes, A. Bergmann, H. Holthusen, Aeroacoustic wind tunnel design, CEAS Aeronaut. J. 10 (1) (2019) 231–249, http://dx.doi.org/10.1007/s13272-019-00372-7.

[6] M. Herr, Design criteria for low-noise trailing-edges, in: 13th AIAA/CEAS Aeroacoustics Conference (28th AIAA Aeroacoustics Conference), American Institute of Aeronautics and Astronautics, 2007, http://dx.doi.org/10.2514/6.2007-3470.

[7] S. Oerlemans, Wind Turbine Noise: Primary Noise Sources, Tech. Rep. NLR-TP-2011-066, National Aerospace Laboratory NLR, 2011.

[8] C. Doolan, D. Moreau, L. Brooks, Wind turbine noise mechanisms and some concepts for its control, Acoust. Aust./Aust. Acoust. Soc. 40 (2012) 7–13.

[9] S. Oerlemans, M. Fisher, T. Maeder, K. Kügler, Reduction of wind turbine noise using optimized airfoils and trailing-edge serrations, AIAA J. 47 (6) (2009) 1470–1481, http://dx.doi.org/10.2514/1.38888.

[10] EASA, Study on the Societal Acceptance of Urban Air Mobility in Europe, Tech. Rep., European Union Aviation Safety Agency, 2021.

[11] S.A. Rizzi, D.L. Huff, D. Douglas Boyd Jr., P. Bent, B.S. Henderson, K.A. Pascioni, D.C. Sargent, D.L. Josephson, M. Marsan, H.B. He, R. Snider, Urban Air Mobility Noise: Current Practice, Gaps, and Recommendations, Tech. Rep. NASA/TP 2020-5007433, NASA, 2020.

[12] K. Brown, W. Devenport, A. Borgoltz, Exploitation of hybrid anechoic wind tunnels for aeroacoustic and aerodynamic measurements, CEAS Aeronaut. J. 10 (1) (2019) 251–266, http://dx.doi.org/10.1007/s13272-019-00385-2.

[13] M. Szoke, C.J. Bahr, F.V. Hutcheson, W.J. Devenport, Characterization of hybrid wind tunnel environments using laser-induced acoustic sources, in: AIAA Scitech 2020 Forum, American Institute of Aeronautics and Astronautics, 2020, http://dx.doi.org/10.2514/6.2020-1253.

[14] M.P.J. Sanders, C.F.J. Koenjer, L. Botero-Bolivar, F.L. dos Santos, C.H. Venner, L.D. de Santana, Trailing-edge noise comparability in open, closed, and hybrid wind tunnel test sections, AIAA J. 60 (7) (2022) 4053–4067, http://dx.doi.org/10.2514/1.j061460.

[15] L. Koop, S. Kroeber, T. Ahlefeldt, K. Ehrenfried, C. Spehr, A. Lauterbach, Microphone-array measurements in wind tunnels: Challenges and limitations, in: Berlin Beamforming Conference 2012, 2012.

[16] S. Kroeber, M. Hellmold, L. Koop, The current understanding of the spectral broadening effect by turbulent shear layers, in: AIA-DAGA 2013 Conference on Acoustic, 2013, pp. 1918–1921.

[17] S. Kroeber, K. Ehrenfried, L. Koop, A. Lauterbach, A. Henning, Systematic comparison of microphone array measurements in open and closed wind tunnels, in: 16th AIAA/CEAS Aeroacoustics Conference, American Institute of Aeronautics and Astronautics, 2010, http://dx.doi.org/10.2514/6.2010-3734.

[18] S. Kroeber, L. Koop, Comparison of microphone array measurements of an airfoil with high-lift devices in open and closed wind tunnels, in: 17th AIAA/CEAS Aeroacoustics Conference (32nd AIAA Aeroacoustics Conference), American Institute of Aeronautics and Astronautics, 2011, http://dx.doi.org/10.2514/6.2011-2721.

[19] S. Oerlemans, P. Sijtsma, Acoustic array measurements of a 1:10.6 scaled airbus A340 model, in: 10th AIAA/CEAS Aeroacoustics Conference, American Institute of Aeronautics and Astronautics, 2004, http://dx.doi.org/10.2514/6.2004-2924.

[20] H.H. Brouwer, Anechoic Wind Tunnels, Tech. Rep. NLR-TP-1997-517, National Aerospace Laboratory NLR, 1997.

[21] A. Lauterbach, K. Ehrenfried, S. Loose, C. Wagner, Microphone array wind tunnel measurements of Reynolds number effects in high-speed train aeroacoustics, Int. J. Aeroacoustics 11 (3–4) (2012) 411–446, http://dx.doi.org/10.1260/1475-472x.11.3-4.411.

[22] O. Pires, X. Munduate, O. Ceyhan, M. Jacobs, H. Snel, Analysis of high Reynolds numbers effects on a wind turbine airfoil using 2D wind tunnel test data, J. Phys. Conf. Ser. 753 (2016) http://dx.doi.org/10.1088/1742-6596/753/2/022047.

[23] Blokhintsev, Acoustics of a Nonhomogeneous Moving Medium, Tech. Rep. NACA-TM-1399, (Translation), 1946.

[24] E. Sarradj, A fast ray casting method for sound refraction at shear layers, in: 22nd AIAA/CEAS Aeroacoustics Conference, American Institute of Aeronautics and Astronautics, 2016, http://dx.doi.org/10.2514/6.2016-2762.

[25] J.A.R. Oliveira, A. Baltazar, M. Castelán, On ray tracing for sharp changing media, J. Acoust. Soc. Am. 146 (3) (2019) 1595–1604, http://dx.doi.org/10.1121/1.5125133.

[26] P. Uginčius, Ray acoustics and Fermat's principle in a moving inhomogeneous medium, J. Acoust. Soc. Am. 51 (5B) (1972) 1759–1763, http://dx.doi.org/10.1121/1.1913024.

[27] L. Koop, K. Ehrenfried, S. Kroeber, Investigation of the systematic phase mismatch in microphone-array analysis, in: 11th AIAA/CEAS Aeroacoustics Conference, American Institute of Aeronautics and Astronautics, 2005, http://dx.doi.org/10.2514/6.2005-2962.

[28] P. Gottlieb, Sound source near a velocity discontinuity, J. Acoust. Soc. Am. 32 (1960) 1117–1122.

[29] R. Amiet, Correction of open jet wind tunnel measurements for shear layer refraction, in: 2nd Aeroacoustics Conference, American Institute of Aeronautics and Astronautics, 1975, http://dx.doi.org/10.2514/6.1975-532.

[30] R. Amiet, Correction of Open-Jet Wind-Tunnel Measurements for Shear Layer Refraction, in: Aeroacoustics: Acoustic Wave Propagation; Aircraft Noise Prediction; Aeroacoustic Instrumentation, American Institute of Aeronautics and Astronautics, 1976, pp. 259–280, http://dx.doi.org/10.2514/5.9781600865206.0259.0280.

[31] H.E. Plumbee, Effects of Forward Velocity on Turbulent Jet Mixing Noise, Tech. Rep. NASA CR-2702, NASA, 1976.

[32] K. Ahuja, B. Tester, H. Tanna, N. Searle, An experimental study of transmission, reflection and scattering of sound in a free-jet flight simulation facility and comparison with theory, in: 4th Aeroacoustics Conference, American Institute of Aeronautics and Astronautics, 1977, http://dx.doi.org/10.2514/6.1977-1266.

[33] C. Bahr, N.S. Zawodny, T. Yardibi, F. Liu, D. Wetzel, B. Bertolucci, L. Cattafesta, Shear layer time-delay correction using a non-intrusive acoustic point source, Int. J. Aeroacoustics 10 (5–6) (2011) 497–530, http://dx.doi.org/10.1260/1475-472X.10.5-6.497.

[34] C. Morfey, P. Joseph, Shear layer refraction corrections for off-axis sources in a jet flow, J. Sound Vib. 239 (4) (2001) 819–848, http://dx.doi.org/10.1006/jsvi.2000.3218.

[35] R. Porteous, T. Geyer, D.J. Moreau, C.J. Doolan, A correction method for acoustic source localisation in convex shear layer geometries, Appl. Acoust. 130 (2018) 128–132, http://dx.doi.org/10.1016/j.apacoust.2017.09.020.

[36] S.M. Candel, Numerical solution of conservation equations arising in linear wave theory: Application to aeroacoustics, J. Fluid Mech. 83 (3) (1977) 465–493, http://dx.doi.org/10.1017/s0022112077001293.

[37] C.K.W. Tam, L. Auriault, Mean flow refraction effects on sound radiated from localized sources in a jet, J. Fluid Mech. 370 (1998) 149–174, http://dx.doi.org/10.1017/s0022112098001852.

[38] S.M. Candel, Sound source radiation in two-dimensional shear flow, AIAA J. 21 (2) (1983) 221–227, http://dx.doi.org/10.2514/3.8057.

[39] T. Padois, C. Prax, V. Valeau, Numerical validation of shear flow corrections for beamforming acoustic source localisation in open wind-tunnels, Appl. Acoust. 74 (4) (2013) 591–601, http://dx.doi.org/10.1016/j.apacoust.2012.09.013.

[40] S. Redonnet, J. Bulte, Numerical investigation of the refraction effects by jet flows in anechoic wind tunnels, with application to NASA/LaRC quiet flow facility, in: 21st AIAA/CEAS Aeroacoustics Conference, American Institute of Aeronautics and Astronautics, 2015, http://dx.doi.org/10.2514/6.2015-3268.

[41] S. Redonnet, Investigation of the acoustic installation effects of an open-jet anechoic wind tunnel using computational aeroacoustics, Appl. Acoust. 169 (2020) 107469, http://dx.doi.org/10.1016/j.apacoust.2020.107469.

[42] D. Casalino, Finite element solutions of a wave equation for sound propagation in sheared flows, AIAA J. 50 (1) (2012) 37–45, http://dx.doi.org/10.2514/1.j050772.

[43] J. Jiao, J. Delfs, J. Dierke, Towards CAA based acoustic wind tunnel corrections for realistic shear layers, in: 21st AIAA/CEAS Aeroacoustics Conference, American Institute of Aeronautics and Astronautics, 2015, http://dx.doi.org/10.2514/6.2015-3278.

[44] J. Jiao, Aeroacoustic Wind Tunnel Correction Based on Numerical Simulation (Ph.D. thesis), TU Braunschweig, 2017.

[45] S.W. Rienstra, A. Hirschberg, An Introduction to Acoustics, 2021.

[46] L. Evans, Partial Differential Equations, American Mathematical Society, Providence, R.I, ISBN: 9780821849743, 2010.

[47] X. Buye, Generalized Acoustic Energy Density and its Applications (Ph.D. thesis), Brigham Young University, 2010.

[48] D. Blokhintzev, The propagation of sound in an inhomogeneous and moving medium I, J. Acoust. Soc. Am. 18 (2) (1946) 322–328, http://dx.doi.org/10.1121/1.1916368.

[49] M.M. Boone, E.A. Vermaas, A new ray-tracing algorithm for arbitrary inhomogeneous and moving media, including caustics, J. Acoust. Soc. Am. 90 (4) (1991) 2109–2117, http://dx.doi.org/10.1121/1.401638.

[50] M. Falcone, The minimum time problem and its applications to front propagation, in: Motion by Mean Curvature and Related Topics, De Gruyter, 1991, http://dx.doi.org/10.1515/9783110870473.70.

[51] H. Görtler, Berechnung von Aufgaben der freien Turbulenz auf Grund eines neuen Näherungsansatzes, ZAMM - Z. Angew. Math. Mech. 22 (5) (1942) 244–254, http://dx.doi.org/10.1002/zamm.19420220503.

[52] F.H. Champagne, Y.H. Pao, I.J. Wygnanski, On the two-dimensional mixing region, J. Fluid Mech. 74 (2) (1976) 209–250, http://dx.doi.org/10.1017/s0022112076001778.

[53] H.W. Liepmann, J. Laufer, Investigations of Free Turbulent Mixing, Tech. Rep., National Advisory Committee for Aeronautics, 1947.

[54] J. Biesheuvel, M. Tuinstra, L.D. de Santana, C. Venner, Finite thickness effects and corrections for acoustic waves propagating through shear layers, in: AIAA AVIATION 2021 FORUM, American Institute of Aeronautics and Astronautics, 2021, http://dx.doi.org/10.2514/6.2021-2130.

[55] E. Sarradj, Three-dimensional acoustic source mapping with different beamforming steering vector formulations, Adv. Acoust. Vib. 2012 (2012) 1–12, http://dx.doi.org/10.1155/2012/292695.

[56] V. Ostashev, D. Hohenwarter, K. Attenborough, P. Blanc-Benon, D. Juvé, G. Goedecke, On the refraction law for a sound ray in a moving medium, Acta Acust. United Acust. 87 (2001) 303–306.

[57] D. Hohenwarter, F. Jelinek, Snell's law of refraction and sound rays for a moving medium, J. Acoust. Soc. Am. 105 (2) (1999) 1387–1388, http://dx.doi.org/10.1121/1.426558.
[58] S.D. Cohen, A.C. Hindmarsh, CVode, a Stiff/Nonstiff ODE Solver in C, Tech. Rep. UCRL-JC-121014. Rev. 1, Stanford University and Lawrence Livermore National Laboratory, 1995.
[59] J.A. Nelder, R. Mead, A simplex method for function minimization, Comput. J. 7 (4) (1965) 308–313, http://dx.doi.org/10.1093/comjnl/7.4.308.